Title
Modeling the Effect of Material Properties on Liquid-Alkaline Water Electrolysis

Journal
Journal of The Electrochemical Society, 171(8)

ISSN
0013-4651

Authors
Lees, Eric W
Bui, Justin C
Wang, Guanhzi
et al.

Publication Date
2024-08-01

DOI
10.1149/1945-7111/ad6bc5

Journal of The Electrochemical Society

Modeling the Effect of Material Properties on Liquid-Alkaline Water Electrolysis

To cite this article: Eric W. Lees *et al* 2024 *J. Electrochem. Soc.* **171** 084502

Journal of The Electrochemical Society, 2024 **171** 084502

Modeling the Effect of Material Properties on Liquid-Alkaline Water Electrolysis

Eric W. Lees,[1] Justin C. Bui,[2] Guanhzi Wang,[1] Hailey R. Boyer,[1,2] Xiong Peng,[1] Alexis T. Bell,[2] and Adam Z. Weber[1,*,z]

[1]*Energy Technologies Area, Lawrence Berkeley National Laboratory, Berkeley, California 94720, United States of America*
[2]*Department of Chemical and Biomolecular Engineering, University of California Berkeley, Berkeley, California 94720, United States of America*

Liquid-alkaline water electrolyzers (LAWEs) use electricity to drive the conversion of water to H_2 and O_2 gas. These devices benefit from the use of low-cost nickel electrodes and metal-oxide separators, but suffer from lower current densities and higher cell voltages than proton-exchange-membrane water electrolyzers. Identifying the inefficiencies that result in this poor performance is key to mitigating losses and optimizing LAWEs. Here, we report an experimentally-validated 1-D continuum model of a LAWE that elucidates the gradients within the cell, simulates H_2 crossover, and projects the energy improvements made possible by modulating the properties of the electrodes and separator. The model captures the Nernstian polarization losses and the distribution of gas- and liquid-phases within the electrodes, enabling quantification of energy losses associated with kinetic, ohmic, and bubble-induced (mass-transport) resistances. Simulations demonstrate that LAWE can achieve energy intensities of 50 kWh kg^{-1} of H_2 at 1 A cm^{-2} using improved electrode and separator properties.

 [DOI: 10.1149/1945-7111/ad6bc5]

Manuscript submitted June 10, 2024; revised manuscript received July 30, 2024. Published August 16, 2024. *This paper is part of the JES Focus Issue on Celebrating Electrochemistry and Electrochemical Engineering at Case Western Reserve University.*

Supplementary material for this article is available online

Water electrolysis is a proven method for electrochemically converting water to H_2 and O_2 gas, thereby storing renewable electrical energy as chemical energy.[1] The H_2 produced by water electrolysis can be stored under pressure during periods when the production of electricity exceeds demand and then used in a fuel cell to produce power during electricity deficits,[2,3] or combined with N_2 or CO_2 gas to synthesize commodity chemicals such as ammonia, ethylene, and sustainable aviation fuel. The cost of H_2 produced by water electrolysis is dictated by electricity costs and the voltage required to drive water electrolysis at high current densities (*i.e.,* >1 A cm^{-2}). This cost of H_2 produced by LAWE must be competitive with the cost of producing H_2 by steam-methane reforming ($1.06 kg^{-1} H_2)[4] to enable widespread deployment of clean H_2 and meet the hydrogen Energy Earthshot target of $1 kg^{-1} H_2.[5]

Liquid-alkaline water electrolyzers (LAWEs) have been used to produce H_2 in industry using excess electricity since the early 20th century. These devices benefit from the use of highly-stable and inexpensive nickel electrodes that are used to catalyze the anodic oxygen-evolution reaction (OER: Eq. 1) and cathodic hydrogen-evolution reaction (HER; Eq. 2). However, LAWEs achieve lower current densities than proton-exchange-membrane water electrolyzers (PEMWEs) (Fig. 1a) due to integrated design and faster transport of protons relative to hydroxides.[6] LAWEs also suffer from performance losses caused by bubble accumulation in the porous electrodes and safety issues associated with crossover of H_2 during current cycling and pressurization,[7] which are necessary operation requirements for LAWEs to respond to changes when coupled with renewable electricity sources.[8] Despite these issues that negatively impact the energy efficiency of LAWEs, LAWEs are more commercialized than PEMWEs. Therefore, an opportunity exists to optimize electrode and separator architectures for LAWEs to manage ohmic, kinetic, and bubble resistances and close the performance gap between PEMWEs and LAWEs.

$$2OH^- \rightarrow \frac{1}{2}O_2 + H_2O + 2e^- \quad U^0_{OER} = 1.23 \text{ V vs RHE} \qquad [1]$$

$$2H_2O + 2e^- \rightarrow H_2 + 2OH^- \quad U^0_{HER} = 0.00 \text{ V vs RHE} \qquad [2]$$

A competent mathematical model is necessary to navigate the expansive design space of electrodes, separators, and operating conditions for LAWEs. Zero-dimensional (0-D) models have been developed that consider the effects of temperature, electrolyte composition, and pressure on the equilibrium cell potential, ohmic resistance, and overpotential of LAWEs.[9–11] However, these 0-D models do not describe ion transport or account for pH gradients throughout the cell, which are impacted by the transport properties (*i.e.,* porosity) of the electrodes and separators. 0-D models neglect these gradients by defining the total kinetic overpotential based on the equilibrium cell potential. The kinetic parameters for HER and OER (*i.e.,* exchange current densities and transfer coefficients) that are fit by 0-D models include lumped kinetic contributions from the OER and HER that are convoluted with concentration polarization effects at the electrodes, which occur because of gradients within the cell. To model a LAWE device rigorously, one must capture these gradients to define the equilibrium for each half-reaction correctly, and how that equilibrium potential varies as a function of operating conditions (*i.e.*, Nernstian shift).

In this paper, we report an experimentally validated 1-D continuum model of a LAWE (Fig. 1b). This model uses the Nernst-Planck equation to define the ion fluxes through the porous electrodes and separator and Tafel kinetics to determine the rates of OER and HER. We accounted for the activity coefficients of water and OH^- using a recently published protocol[12] to determine accurately the local pH and overpotential throughout the electrodes. The model reveals gradients in pH, conductivity, and water saturation in LAWEs and deconvolutes the applied voltage into kinetic, ohmic, and polarization losses. Gradients within the electrolyzer are shown to impact the equilibrium potential and reaction kinetics at the electrodes. We demonstrate the utility of the model by applying it to LAWE data collected with nickel-foam and nickel-felt electrodes to explore the effect of electrode properties (*e.g.,* surface area and porosity) and separator thickness on the tradeoff between the energy-

*Electrochemical Society Fellow.
[z]E-mail: azweber@lbl.gov

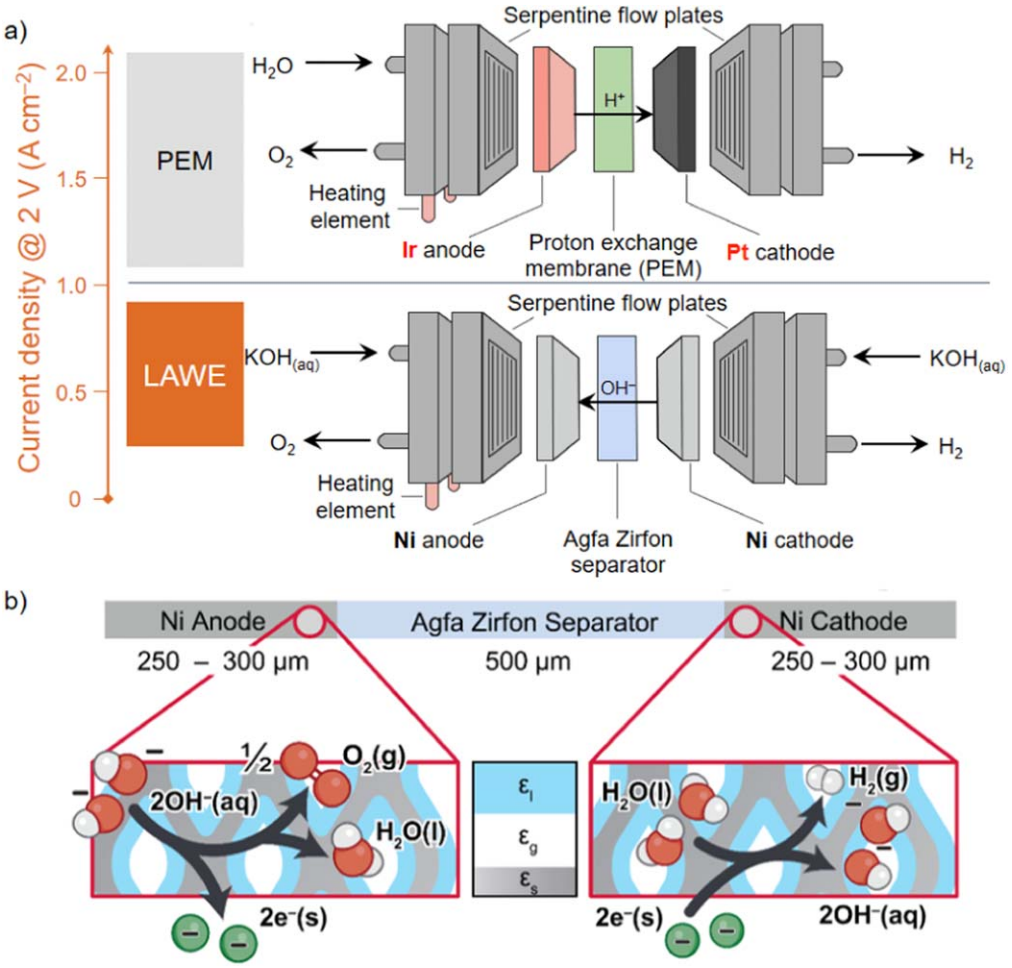

Figure 1. (a) Diagram showing the nominal operating current density and architecture of a liquid-alkaline water electrolyzer (LAWE) compared to a proton-exchange-membrane water electrolyzer (PEMWE). (b) Schematic diagram of the 1-D continuum model showing the different phases present and the reaction chemistry.

intensity of H_2 production and the crossover of H_2 gas from cathode to anode.

Theoretical Model

Definition of pH.—LAWEs typically used concentrated NaOH/KOH as the electrolyte (e.g., 7 M).[13] At this high concentration, the ions are not entirely solvated and non-ideal solution behavior occurs. Accordingly, the pH is defined by the activities of ions present in the solution,[12]

$$\mathrm{pH} = -\log K_W - \log \frac{a_{\mathrm{H_2O}}}{\gamma_{\mathrm{OH^-}} m} \quad [3]$$

where $a_{\mathrm{H_2O}}$ is the activity of water, m is the solution molality (mol $_{\mathrm{KOH}}$ $\mathrm{kg_{H_2O}}^{-1}$), $\gamma_{\mathrm{OH^-}}$ is the activity coefficient of OH^-, and K_W is the equilibrium coefficient for the water dissociation reaction,[12]

$$\log(K_w) = -3.0039 \times 10^{-9} T^4 + 1.1302 \times 10^{-6} T^3 - 2.481 \times 10^{-4} T^2 + 0.04338416 T - 14.94571088 \quad [4]$$

The temperature (T) and compositional dependences of the water and hydroxide activities were measured using electromotive force measurements as reported by Åkerlöf et al.,[14,15]

$$\log \gamma_{\mathrm{OH^-}} = \frac{-u\sqrt{m}}{1+\sqrt{2m}} + Bm + Cm^2 + Dm^3 + Em^4 \quad [5]$$

$$\log a_{\mathrm{H_2O}} = \frac{-2m}{2.303 * 55.51} + \frac{u}{55.51 \cdot \sqrt{2}} \left[1 + \sqrt{2m} - 2\ln(1+\sqrt{2m}) - \frac{1}{1+\sqrt{2m}}\right] - \frac{2}{55.51}\left(\frac{Bm^2}{2} + \frac{2Cm^3}{3} + \frac{3Dm^4}{4} + \frac{4Em^5}{5}\right) \quad [6]$$

Where u is the universal constant of the limiting law, and B, C, D, and E are empirical parameters that depend on temperature in degrees Celsius,

$$u = 0.486 + 6.9 \times 10^{-4} T + 8.14 \times 10^{-7} T^2 + 1.15 \times 10^{-7} T^3 - 5.68 \times 10^{-10} T^4 \quad [7]$$

$$B = 0.06629 + 0.0006135 T - 0.000011018 T^2 + 0.000000004096 T^3 \quad [8]$$

$$C = 0.010909 - 0.00017108 T + 0.0000016895 T^2 - 0.0000000007969 T^3 \quad [9]$$

$$D = -0.0007351 + 0.0000099737T - 0.00000009347T^2 + 0.0000000006215T^3 \quad [10]$$

$$E = 0.000015502 - 0.0000001987T + 0.0000000018424T^2 - 0.000000000017647T^3 \quad [11]$$

The molality (m_{KOH}) in units is related to the concentration of KOH (c_{KOH}) and its density (ρ_{KOH})

$$m_{KOH} = \frac{\frac{c_{KOH}M_{KOH}}{\rho_{KOH}}}{M_{KOH}\left(1 - \frac{c_{KOH}M_{KOH}}{\rho_{KOH}}\right)} \quad [12]$$

Where M_{KOH} is the molar mass of KOH. ρ_{KOH} is calculated as a function of density using a 3rd order polynomial fit of experimental data (shown below for),[16]

$$\rho_{KOH} = 2.98215 \times 10^{-5}c_{KOH}^3 - 0.001154326c_{KOH}^2 + 0.048435198c_{KOH} + 0.972262119 \quad [13]$$

Where ρ_{KOH} and c_{KOH} have units of kg m^{-3} and M, respectively.

Governing equations.—The 1-D continuum domain was designed to resemble a standard zero-gap LAWE architecture consisting of porous anode, separator, and cathode domains (Fig. 1b). The transport of dissolved species i (OH^-, K^+, H^+, $O_{2(aq)}$, and $H_{2(aq)}$) was modeled throughout the electrodes and separator using a differential mole balance,

$$\nabla \cdot n_i = \varepsilon_L \sum_i R_{W,i} + \sum_i R_{CT,i} + \sum_i R_{PT,i} \quad [14]$$

where n_i is the flux of species i and ε_L is the volume fraction of the porous electrode or separator occupied by aqueous KOH solution. $R_{CT,i}$ and $R_{W,i}$ are the source terms for of species i associated with charge transfer reactions (*i.e.*, the OER and HER) and water dissociation/recombination, respectively. $R_{PT,i}$ is the rate of transport of O_2 and H_2 between the liquid- and gas-phases, which is given by,

$$R_{PT,i} = k_{MT}(c_i - H_i p_i) \quad [15]$$

where k_{MT} is the gas-liquid mass transfer coefficient, c_i is the concentration of dissolved species i, H_i is the Henry's constant of species i, and p_i is the partial pressure of species i. The Henry's constants of dissolved O_2 and H_2 were determined as a function of concentration and temperature using the polynomial fits reported by Hodges et al.[17] The gas-liquid mass transfer coefficient k_{GL} was estimated based on the diffusion coefficient of dissolved O_2 or H_2 (D_i),[17] nominal radius of the nickel fibers (r_f), and the water saturation (S_L) using a Fick's Law correlation reported by Weng et al.[18] with square-root dependences on the total current density and gas pressure as reported by Kraakman et al.,[19]

$$k_{GL} = f i_{total}^{0.5} p_G^{-0.5} \frac{D_i}{L_{BL}(1 - \sqrt{1 - S_L})} \quad [16]$$

where f is a fitted parameter obtained from Kraakman et al.[19] and L_{BL} is the nominal boundary layer thickness. The dependence of the mass-transfer coefficient on the reciprocal of the square-root of pressure arises from the increased bubble-holdup at elevated pressures. The square-root dependence on the total current density is associated with bubble-induced convection, which reduces the mass-transfer boundary layer.[20,21]

The Nernst-Planck equation (with consideration of convection) was used to determine the flux of dissolved species in the pores of the electrode and separator,

$$n_i = -D_i^{eff}\left(\nabla c_i + z_i \frac{F}{RT} c_i \nabla \phi_I\right) + c_i u_L \quad [17]$$

Where z_i is the charge of the species i, c_i is the concentration of species i, F is Faraday's constant (96485 C mol^{-1}), R is the ideal gas constant (8.314 J mol^{-1} K^{-1}), D_i^{eff} is the effective diffusion coefficient, u_L is the mass-averaged velocity in the liquid-phase, andϕ_I is the electrolyte potential. For dissolved H_2 and O_2, the migration term in Eq. 17 is zero, and thus, only diffusion and convection contribute to the net flux of these species. The Peclet number associated with liquid-phase transport of OH^- is defined here as the ratio between the magnitude of the convective and diffusive fluxes,

$$Pe_L = \frac{|c_{OH^-}u_L|}{|-D_{OH^-}^{eff}\nabla c_{OH^-}|} \quad [18]$$

The electrolyte potential was determined by the electroneutrality closure relationship,

$$\sum_i z_i c_i = 0 \quad [19]$$

The transport of gaseous species j ($O_{2(g)}$ and $H_{2(g)}$) was modeled using mass conservation,

$$\nabla \cdot J_j = -\sum_j M_j R_{PT,j} \quad [20]$$

where J_j is the mass flux of species j, M_j is the molecular weight of species j, and $R_{PT,j}$ is the rate of phase-transfer for species j. The mass flux is defined using a mixture-averaged approach,

$$J_j = -\rho_g D_j^{eff}\nabla\omega_j - \rho_G D_j^{eff}\omega_j \frac{\nabla M_n}{M_n} + \rho_j u_G \quad [21]$$

where ρ_g is the density of the gas-phase, ω_j is the mass fraction of species j, M_n is the mass-averaged molecular weight, ρ_j is the mass concentration of species j, and u_G is the mass-averaged velocity of the gas-phase. The effective diffusion coefficients (D_j^{eff}) were determined based on a traditional parallel resistor model which accounts for contributions from the mixed molecular diffusion coefficients (D_j^m) and Knudsen diffusion coefficients (D_j^k). To account for porosity and tortuosity, the effective diffusion coefficient was modified by the Bruggeman correlation,

$$D_j^{eff} = (1 - \varepsilon_L)^{1.5}\left(\frac{1}{D_j^m} + \frac{1}{D_j^k}\right)^{-1} \quad [22]$$

$$D_j^k = \frac{2\lambda_{path}}{3}\sqrt{\frac{8RT}{\pi M_i}} \quad [23]$$

where λ_{path} is the mean free path in the pores of the electrode. The molecular diffusion coefficient of O_2 in H_2 (D_{O_2,H_2}) was determined using the diffusion volume correlation introduced by Fuller et al.,[22]

$$D_{O_2,H_2} = \frac{10^{-3}T[K]^{1.75}(M_{O_2}[\text{g mol}^{-1}]^{-1} + M_{H_2}[\text{g mol}^{-1}]^{-1})^{0.5}}{p_G[\text{atm}](\nu_{p,O_2}^{0.33} + \nu_{p,H_2}^{0.33})^2} \quad [24]$$

where ν_{H_2} and ν_{O_2} are the diffusion volumes of H_2 and O_2. The mixture-averaged molecular diffusion coefficients are given by,

$$D_j^{\mathrm{m}} = \frac{1 - \omega_j}{\sum_{n \neq j} \frac{y_n}{D_{j,n}}} \quad [25]$$

where y_n is the mole fraction of species n.

Conservation of electrical charge was applied to the solid-fraction of the porous electrodes and the transport of electrons is governed by Ohm's law,

$$\nabla \cdot i_s = -F \sum_i z_i R_{CT,i} \quad [26]$$

$$\mathrm{i}_s = -\nabla \cdot \left(\frac{1}{r_{\mathrm{eff}}} \phi_s \right) \quad [27]$$

where i_s is the electrical current density and ϕ_s is the electric potential (*i.e.,* the potential through the electron conducting phase). The effective electrical resistance (r^{eff}) of the nickel-foam electrodes was determined using the correlation given by Liu et al.[23]

$$r^{\mathrm{eff}} = 3r^0 \frac{1 - 0.121(1 - \varepsilon_1)^{\frac{1}{2}}}{1 - \varepsilon_1} \quad [28]$$

where r^0 is the resistivity of nonporous nickel.

Ionic conductivity model.—Given the strong correlation between LAWE performance and separator properties (*e.g.,* thickness),[24] it is necessary for the modeled ionic conductivities to match areal resistance (AR) measurements. Therefore, the effective diffusion coefficient for OH^- and K^+ were determined based on the effective conductivity (κ^{eff}) of either the separator or the electrodes,

$$D_i^{\mathrm{eff}} = \frac{t_i \kappa^{\mathrm{eff}} RT}{{z_{\mathrm{i}}}^2 F^2 c_{\mathrm{i}}} \quad [29]$$

where t_i is the transference number for OH^- and K^+.[25] The κ^{eff} in the electrodes was determined by correcting the bulk conductivity of KOH (κ_{KOH})[26] for the volume fraction of liquid (ε_L) using the Bruggeman correlation,

$$\kappa^{\mathrm{eff}} = \varepsilon_L^{1.5} \kappa_{\mathrm{KOH}} \quad [30]$$

$$\begin{aligned} \kappa_{\mathrm{KOH}} = & -2.04 c_{\mathrm{KOH}} - 2.8 \times 10^{-3} c_{\mathrm{KOH}}^2 + 5.33 \\ & \times 10^{-3} c_{\mathrm{KOH}} T + 207 \frac{c_{\mathrm{KOH}}}{T} + 1.04 \\ & \times 10^{-3} c_{\mathrm{KOH}}^3 - 3 \times 10^{-7} c_{\mathrm{KOH}}^2 T^2 \end{aligned} \quad [31]$$

The ohmic resistance of the separator was determined by considering the tortuosity (τ) of the separator,[27]

$$\kappa^{\mathrm{eff}} = \frac{\varepsilon_{\mathrm{L}}}{\tau} \kappa_{\mathrm{KOH}} \quad [32]$$

The modeled areal resistance (AR) of the membrane was determined as,

$$\mathrm{AR} = \int_{L_{anode}}^{L_{anode}+L_{sep}} \frac{1}{\kappa^{\mathrm{eff}}} dx \quad [33]$$

where L_{sep} is the separator thickness and L_{anode} is the anode thickness (*i.e.,* the electrode thickness).

Hydrogen and oxygen evolution reaction kinetics.—The charge-transfer source terms for OH^- are determined based on the stoichiometry of reaction k (i.e., the OER and HER),

$$R_{CT,\mathrm{i}} = -M_i \frac{a_v s_{i,k} i_k}{n_k F} \quad [34]$$

where M_i is the molar mass of species i, $s_{i,k}$ is the stoichiometric coefficient of species i in reduction reaction k (where reduced species have positive stoichiometric coefficients and oxidized species have negative stoichiometric coefficients), and n_k is the number of electrons transferred in reaction k. The nominal specific surface area ($a_{v,0}$) is the is given by the following correlation for nickel-foam that is based on the ideal tetradecahedron model for metallic foams,[28]

$$a_{v,0} = \frac{30.03}{\mathrm{d}_{\mathrm{foam}}} [2.74(1 - \varepsilon_L^0)^{\frac{1}{2}} - (1 - \varepsilon_L^0)](1 - \varepsilon_L^0)^{-1.4979} \quad [35]$$

where the value of 30.03 and exponent of −1.4979 are fitted values specific to nickel-foam, and d_{foam} and ε_L^0 are the average pore diameter and nominal porosity of the foam, respectively. The local volumetric current densities for the OER ($i_{\mathrm{OER,v}}$) and HER ($i_{\mathrm{HER,v}}$) are given as Tafel expressions,

$$i_{\mathrm{OER,v}} = a_v i_{0,\mathrm{OER}} a_{OH^-} \exp\left(\frac{\alpha_{a,\mathrm{OER}} F}{RT} \eta_{\mathrm{OER}} \right) \quad [36]$$

$$i_{\mathrm{HER,v}} = -a_v i_{0,\mathrm{HER}} \exp\left(-\frac{\alpha_{c,\mathrm{HER}} F}{RT} \eta_{\mathrm{HER}} \right) \quad [37]$$

where a_v is the effective specific surface area of the electrodes, $i_{0,\mathrm{OER}}$ is the exchange current density for the OER and $i_{0,\mathrm{HER}}$ is the exchange current density for the HER. $\alpha_{a,\mathrm{OER}}$ and $\alpha_{c,\mathrm{HER}}$ are the charge-transfer coefficients for the OER and HER, respectively, obtained from Harverkort et al.[29] The kinetic overpotentials for the OER (η_{OER}) and HER (η_{HER}) are defined by the reversible cell potential for the OER or HER (U_k^0) with consideration of the Nernstian shift caused by changes in pressure, water activity, and pH,

$$\eta_{\mathrm{HER}} = \phi_s - \phi_l - \left(U_{HER}^0 - \frac{2.303RT}{2F} 2\mathrm{pH} + \log(\mathrm{P_{H_2}}) \right) \quad [38]$$

$$\eta_{\mathrm{OER}} = \phi_s - \phi_l - \left(U_{OER}^0 - \frac{2.303RT}{2F} 2\mathrm{pH} - 0.5 \log(\mathrm{P_{O_2}}) + \log(\mathrm{a_{H_2O}}) \right) \quad [39]$$

where the reversible potential for OER is derived from the Gibbs-Helmholtz relationship between the enthalpy and Gibbs Free Energy and defined with respect to a RHE,[30,31]

$$U_{\mathrm{OER}}^0 = 1.50342 - 9.956 \times 10^{-4}\,\mathrm{T} + 2.5 \times 10^{-7}\,\mathrm{T}^2 \quad [40]$$

where T is the temperature in Kelvin. The geometric current densities for HER (i_{HER}) and OER i_{HER}) are calculated by integrating the local volumetric current densities,

$$i_{\mathrm{HER}} = \int_{L_{aCL}+L_{sep}}^{L_{aCL}+L_{sep}+L_{cCL}} i_{\mathrm{HER,v}}\, dx \quad [41]$$

$$i_{\mathrm{OER}} = \int_0^{L_{aCL}} i_{\mathrm{OER,v}}\, dx \quad [42]$$

The total cell potential (V_{cell}) was calculated using the applied potential (V_{app}) with consideration of the contact resistance ($R_{contact}$) between the electrode and flow plate,

$$V_{cell} = V_{app} + i_{total} R_{contact} \quad [43]$$

where i_{total} is the total current density, which is equal to both the HER or OER current density.

Momentum balances and capillary pressure.—The momentum balances on the liquid and gas phases are given as,

$$\nabla \cdot (\rho_G u_G) = Q_G \quad [44]$$

$$\nabla \cdot (\rho_G u_L) = Q_L \quad [45]$$

where Q_G is the net rate of mass generation in the gas-phase. ρ_L, u_L, and Q_L are the density, mass-averaged velocity, and net rate of mass generation in the liquid-phase, respectively. ρ_G, u_G, and Q_G are the density, mass-averaged velocity, and net rate of mass generation in the gas-phase, respectively. The mass generation/consumption source terms are associated with the production of H_2 and O_2 gas,

$$Q_G = \sum_i R_{PT,i} MW_i \quad [46]$$

$$Q_L = \sum_i -R_{PT,i} MW_i \quad [47]$$

The convective velocity of the gas-phase (u_G) and liquid-phase (u_L) was determined using Darcy's law,

$$u_L = -\frac{\kappa_{sat}^0 \kappa_{rL}}{\mu_L} \nabla p_L \quad [48]$$

$$u_G = -\frac{\kappa_{sat}^0 \kappa_{rG}}{\mu_G} \nabla p_G \quad [49]$$

where κ_{sat}^0 is the saturated permeability, μ_G is the viscosity of the gas-phase, and μ_L is the viscosity of the KOH solution. The gas-phase viscosity was estimated using a simple concentration-weighted average of the viscosities of H_2 and O_2,

$$\mu_G = \mu_{H_2} y_{H_2} + \mu_{O_2} y_{O_2} \quad [50]$$

where μ_{H_2} and μ_{O_2} are the viscosities of H_2 and O_2, respectively, and y_{H_2} and y_{O_2} are the mole fractions of H_2 and O_2, respectively, in the gas phase. The relative permeability (κ_{rG}) of the gas-phase and liquid-phase (κ_{rL}) were estimated based on a cubic dependence on water saturation (S_L) used commonly in reservoir engineering and fuel cells,[33][32]

$$\kappa_{rg} = (1 - S_L)^3 \quad [51]$$

$$\kappa_{rL} = S_L^3 \quad [52]$$

The water saturation (S_L) represents the volume fraction of liquid in the pores. The water saturation was defined based on the capillary pressure (p_{cap}) using a Leverett J-function for hydrophobic (non-wetting) materials (*i.e.,* materials with contact angles > 90 degrees),[33]

$$p_{cap} = p_L - p_G \quad [53]$$

$$p_{cap} = -\sigma_{KOH} \cos(\theta) \left(\frac{\varepsilon_{l,0}}{\kappa_{sat}^0}\right)^{0.5} (1.42 S_L - 2.12 S_L{}^2 + 1.26 S_L^3) \quad [54]$$

where σ_{KOH} is the surface tension of the KOH solution, θ is the contact angle in radians, and $\varepsilon_{l,0}$ is the nominal porosity of the electrodes. For the Zirfon separator, which is hydrophilic (*i.e.,* contact angle < 90 degrees), the capillary pressure is defined as

$$p_{cap} = -\sigma_{KOH} \cos(\theta) \left(\frac{\varepsilon_{l,0}}{\kappa_{sep}^0}\right)^{0.5} 1.42(1 - S_L) - 2.12(1 - S_L)^2 + 1.26(1 - S_L)^3 \quad [55]$$

The capillary pressure curves for the electrodes and Zirfon separator are shown in Fig. S1 using relevant parameters for each material defined in Table S2.

The gas entrained in the liquid electrolyte can block surface sites on the electrode and also reduce the electrolyte volume fraction. We considered the active specific surface area (a_v) to be the wetted area of the nickel-foam with the remainder of the surface area covered by bubbles. The fraction of available surface area and electrolyte pathways for ion transfer were assumed to vary linearly with the water saturation in the electrodes,

$$a_v = a_{v,0} S_L \quad [56]$$

$$\varepsilon_L = \varepsilon_{L,0} S_L \quad [57]$$

Water-dissociation equilibrium.—The rate of consumption/generation of species i (H^+ and OH^-) by the water dissociation/recombination reaction ($R_{W,i}$) was modeled as a bulk reaction in the electrolyte to maintain thermodynamic equilibrium between H^+, OH^-, and H_2O. This homogeneous reaction is described by the law of mass action,

$$R_{w,H^+} = \varepsilon_L (k_w a_w - k_{-w} a_{H^+} a_{OH^-}) \quad [58]$$

$$R_{w,OH^-} = \varepsilon_L (k_w a_w - k_{-w} a_{H^+} a_{OH^-}) \quad [59]$$

where k_w (Table S1) and $k_{-w} = \frac{k_w}{K_w}$ are the rate constants.

Boundary conditions.—Dirichlet boundary conditions were used to simulate the 7 M KOH cathode and anode feed streams,

$$c_{OH^-}|_{x=0\ \mu m,\ L_{anode}+L_{sep}+L_{cathode}} = 7\ M \quad [60]$$

$$c_{H^+}|_{x=0\ \mu m,\ L_{anode}+L_{sep}+L_{cathode}} = 10^{-14.1} M \quad [61]$$

$$c_{K^+}|_{x=0\ \mu m,\ L_{anode}+L_{sep}+L_{cathode}} = 7\ M \quad [62]$$

The liquid- and gas-pressure at both the anode/flowplate and cathode/flow plate interfaces were assigned values of,

$$p_L|_{x=0\ \mu m,\ L_{anode}+L_{sep}+L_{cathode}} = p_{op} + p_{cap} \quad [63]$$

$$p_G|_{x=0\ \mu m,\ L_{anode}+L_{sep}+L_{cathode}} = p_{op} \quad [64]$$

where p_{op} is the operating pressure (1 atm for the Base case simulation) and p_{cap} is the capillary pressure which corresponds to a water saturation of 0.9999. This boundary condition implies that the electrodes are completely filled with KOH solution at the electrode/flow plate interface, consistent with neutron imaging studies by Zlobinski et al.[34]

The gas-phase mass flux of H_2 and O_2 at the electrode/flow plate interfaces were determined using an outflow boundary condition,

$$J_j|_{x=0\ \mu m,\ L_{anode}+L_{sep}+L_{cathode}} = \rho_j u_G \quad [65]$$

$$-\rho_g D_j^{eff} \nabla \omega_j = 0 \quad [66]$$

where ω_j is the mass fraction of gaseous species j. This boundary condition implies that there are no concentration gradients at the

anode/flow channel interface (*i.e.,* the channel is filled with the same gas as what exists at the edge of the anode) and therefore convection is the only transport mechanism across this interface.

The dissolved gases were assumed to be in equilibrium with the gas-phase at the electrode/flow plate interface. Therefore, the fluxes of H_2 and O_2 in the electrolyte are defined as,

$$n_{i=H_2\ or\ O_2}|_{x=0\ \mu m,\ L_{anode}+L_{sep}+L_{cathode}} = k_{MT,i}(p_{i,b}H_i - c_i) \quad [67]$$

where $k_{MT,i}$ is the mass-transfer coefficient for species i derived based on correlations for flow perpendicular to a flat plate,

$$k_{MT,i} = 0.664\frac{D_j}{L_{electrode}}\mathrm{Re}_j^{1/2}\mathrm{Sc}_j^{1/3} \quad [68]$$

where D_j is the diffusivity of dissolved H_2 or O_2, $L_{electrode}$ is the length of the electrode. Re_i and Sc_i are the Reynolds number and Schmidt number of species i. $p_{i,b}$ is the partial pressure of dissolved species i in the gas phase. Finally, the anode was set to a reference potential of 0 V and the cathode voltage was set to the applied voltage (V_{app}),

$$\phi|_{x=0\ \mu m} = 0\ V \quad [69]$$

$$\phi|_{x=\ L_{anode}+L_{sep}+L_{cathode}} = V_{app} \quad [70]$$

Where V_{app} was swept from -1.18 to -2.6 V to simulate the experimental polarization curve.

Applied-voltage-breakdown analysis.—A primary feature of electrolyzer models is the ability to deconstruct the total applied voltage into its components.[35] To do so, a power-loss analysis is used to resolve the individual voltage contributions associated with reaction kinetics, mass transfer, and Ohmic resistances. The voltage loss due to the reaction kinetics ($\Delta V_{kinetic}$) is derived from the Tafel equation,

$$\Delta V_{kinetic,\ \mathrm{OER}} = \int_0^{L_{anode}} \frac{\frac{RTi_{\mathrm{OER},v}}{\alpha_{a,\mathrm{OER}}F}\ln\left(\frac{i_{\mathrm{OER},v}}{i_{0,\mathrm{OER}}a_v}\right)}{i_{total}}dx \quad [71]$$

$$\Delta V_{kinetic,\ \mathrm{HER}} = \int_{L_{anode}+L_{sep}}^{L_{anode}+L_{sep}+L_{cathode}} \frac{\frac{-RTi_{\mathrm{HER},v}}{\alpha_{c,\mathrm{HER}}F}\ln\left(\frac{-i_{\mathrm{HER},v}}{i_{0,\mathrm{HER}}a_v}\right)}{i_{total}}dx \quad [72]$$

Where $L_{cathode}$ is the thickness of the cathode. The voltage losses associated with mass transfer (ΔV_{MT}) represent potential losses associated with concentration polarization and are determined based on the difference between the local and bulk concentrations,

$$\Delta V_{MT} = \int_0^{L_{anode}} \frac{\frac{i_{OER,v}RT}{\alpha_{a,\mathrm{OER}}F}\ln\left(\frac{\gamma_{\mathrm{OH}^-}c_{\mathrm{OH}^-}}{\gamma_{\mathrm{OH}^-,\mathrm{bulk}}c_{\mathrm{OH}^-,\mathrm{bulk}}}\right)}{i_{total}}dx \quad [73]$$

The voltage loss due to ionic resistance in the electrodes and separator is determined from Ohm's law in the aqueous phase and is given as

$$\Delta V_{ionic} = \int_0^{L_{anode}+L_{sep}+L_{cathode}} \frac{\nabla\cdot\phi_l i_l}{i_{total}}dx \quad [74]$$

where i_l is the current density in the electrolyte. The voltage loss associated with electron transport in the nickel electrodes is determined from Ohm's law in the solid phase and is given as,

$$\Delta V_{electric} = \int_0^{L_{anode}} \frac{\nabla\cdot\phi_s i_s}{i_{total}}dx + \int_{L_{anode}+L_{sep}}^{L_{anode}+L_{sep}+L_{cathode}} \frac{\nabla\cdot\phi_s i_s}{i_{total}}dx + i_{total}R_{contact} \quad [75]$$

Finally, the overpotential associated with bubble formation was determined by subtracting the current density obtained when bubble formation is considered by the current density obtained without bubble formation. This value represents the voltage loss associated with the loss of surface area and electrolyte volume associated with bubble formation.

Numerical methods and model parameters.—The governing equations representing this model were solved in COMSOL Multiphysics 6.0. The simulations in the present study were solved using the PARallel DIrect SOlver (PARDISO) solver using Newton's Method with a tolerance of 0.001 and a recovery damping factor of 0.35. The 1-D domain was discretized with 50,000 elements to ensure convergence. The parameters used in the model are shown in Tables S1-S3.

Experimental Methods

Electrolyzer architecture and materials.—The electrolyzer used in this study consists of two 5 cm^2 serpentine flow fields, ethylene tetrafluoroethylene (ETFE) gaskets, a Zirfon separator (AGFA Perl UTP 500), and either nickel-foam or nickel-felt electrodes. The electrolyzer assembly was sourced from Fuel Cell Technologies Inc. The nickel-foam electrodes were sourced from MSE Supplies and the nickel-felt electrodes were sourced from Bekaert. The KOH salt (>85%) used to make the electrolyte was purchased from Fisher Chemical. The electrolyte solutions were prepared by adding the KOH to deionized water. The ETFE material used to form the gaskets was purchased from CS Hyde.

Scanning electron microscopy (SEM) images were collected for the nickel-foam and nickel-felt electrodes (Fig. S2) with a Quanta FEG 250 from Thermo Fisher (formally FEI) at an energy of 10 kV. Micrographs of the electrodes were collected prior to electrolysis under high vacuum ($<2\times10^{-5}$ Torr).

Electrolysis experiments.—The electrolyzer was operated at constant current densities ranging from 0 to 2 A cm^{-2} using a Biologic VSP potentiostat. Cell-voltage measurements were determined by averaging the potentials over 20 s of operation. During electrolyzer operation, 7 M KOH was fed to the anode and cathode at a flow rate of 20 ml min^{-1} using a peristaltic pump. The electrolyte reservoir used to store the 7 M KOH was held at a constant temperature of 80 °C. Cartridge heaters embedded in the electrolyzer were also set to 80 °C. To determine the ohmic resistances in the electrolyzer, electrochemical-impedance spectroscopy (EIS) was performed at a frequency range of 1 to 100 kHz at each tested current density. The high-frequency resistance (HFR) was determined by fitting the EIS data with an equivalent-circuit containing a resistor and two resistor-constant phase elements.

The double-layer capacitance (C_{dl}) measured were performed in a three-electrode system with a 1 M KOH electrolyte and the nickel electrodes were used as the working electrodes. A graphite rod was used as the counter electrode and a Ag/AgCl electrode was used as the reference. The double-layer capacitances for the nickel electrodes were determined by performing cyclic voltammetry in non-Faradic potential windows at various scan rates. The double-layer capacitance was then determined as

$$C_{dl} = \frac{i_{dl}}{\nu} \quad [73a]$$

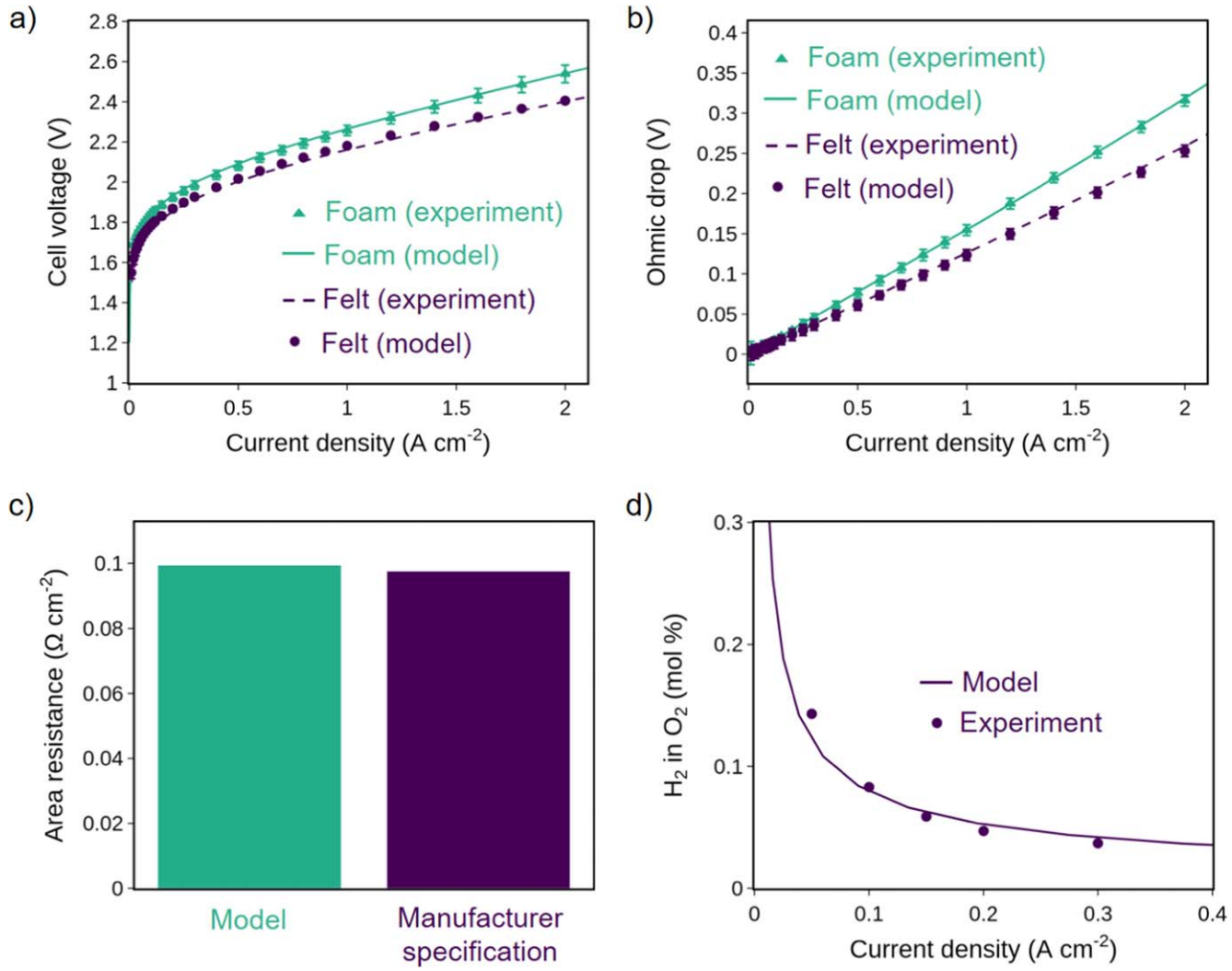

Figure 2. (a) Experimentally-measured and modeled polarization curves for the LAWE operated with nickel-foam and nickel-felt. (b) Experimental and modeled ohmic drops. (c) Comparison of the modeled area resistance to the manufacturer specification for Zirfon PERL UTP 500 separator at 90 °C. (d) Modeled and experimental H_2 in O_2 (mol %) as a function of current density. The experimental values are reported by Haug et al.[38] for a LAWE operated at 1 bar and 80°C using a 30 wt% KOH electrolyte.

where i_{dl} is the double-layer current densities collected from the cyclic voltammetry measurements at the same potential and v is the scan rate. The C_{dl} of the nickel-foam was measured to be 280 μF cm^{-2} whereas the C_{dl} of the nickel-felt was measured to be 660 μF cm^{-2}.

Results and Discussion

Model validation with experimental data.—Electrolyzer experiments were performed at 80 °C, ambient pressure, and constant current densities ranging from 0 to 2 A cm^{-2} using either nickel-foam or nickel-felt as both the anode and cathode. The 1-D continuum model of the cathode, separator, and anode was developed to simulate the electrolyzer performance with each of these electrodes. The transfer coefficients for OER and HER ($\alpha_{a,OER}$ and $\alpha_{c,HER}$) were obtained from literature[29] and the specific surface area of the nickel-foam was calculated using the ideal tetradecahedron model for metal foams (Eq. 35)[28] with the pore diameter estimated using scanning electron microscopy (Fig. S2). The specific surface area of the nickel-felt was estimated by the ratio between the experimentally-measured double-layer capacitances of the nickel-felt and nickel-foam, which was determined to be 2.35. Double-layer capacitance is not a quantitative measure of the absolute specific surface area due to the frequency dependence and influence of surface oxides.[36,37] Given this limitation, the double-layer capacitance experiments were performed using the same material (nickel) under the exact same operating conditions (room temperature with 1 M KOH). Moreover, the ratio of the nickel-foam and nickel-felt electrodes was used as a model parameter because the relative values likely are more accurate. A detailed sensitivity analysis examining the effect of specific surface area is discussed below to understand the impact of this parameter on the simulation results.

The experiments show that the nickel-felt electrodes yield lower cell potentials compared to the nickel-foam electrodes at all tested current densities (Fig. 2a). The model was calibrated by fitting the exchange current densities for the OER ($i_{0,OER}$) and HER ($i_{0,HER}$) to the experimental data collected using the nickel-foam electrodes (See Table S1 for kinetic parameters). The model was then used to predict the performance of the nickel-felt electrodes using the same kinetic parameters used to fit the nickel-foam data but with the nickel-felt properties (Table S2). As shown in Fig. 2a, good agreement is observed between the model predictions and experimental results. These results indicated that the improved performance with the nickel-felt electrodes is enabled, in part, by the 2.35× higher surface area (*i.e.,* double-layer capacitance) relative to the nickel-foam electrodes.

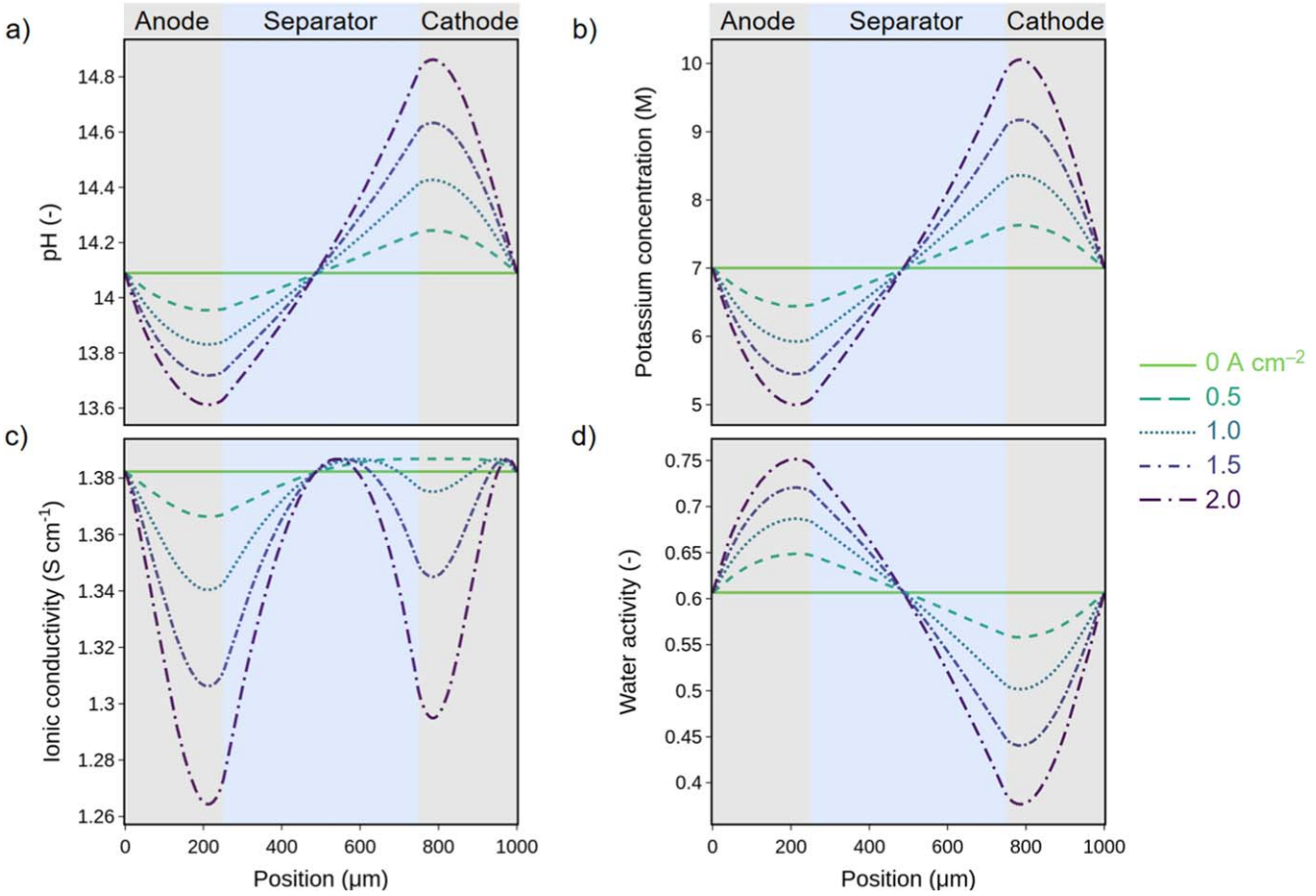

Figure 3. Modeled (a) pH, (b) K^+ concentration (c), KOH conductivity, and (d) water activity as a function of current density and position within the LAWE.

The experimentally measured ohmic drops (determined by electrochemical-impedance spectroscopy (EIS)) show that replacing nickel-foam electrodes with nickel-felt ones reduces the ohmic or high-frequency resistance of the electrolyzer (Fig. 2b). The modeled ohmic drops agree well with the experimental data. Moreover, the simulated area resistance of the Zirfon was compared to the manufacturer specification (Fig. 2c), with nearly identical values. These results confirm that the diffusion coefficients for OH^- used in the Nernst-Planck equation effectively describe the ohmic resistances in the separator.

Given that the same Zirfon separator is used for both the nickel-foam and nickel-felt experiments, the difference in ohmic resistance must be attributed to the differences in ionic and contact resistances between the two types of electrodes. The simulated water saturation in the nickel-felt electrodes (Fig. S3a) is lower than in the nickel-foam electrodes (Fig. S3b) due to the lower effective permeability of the felt electrodes reduces gas transport away from the electrolyte/separator interface. Therefore, the higher water saturation in the foam electrodes compared to the felt electrodes reduces the ohmic drop associated with ion transfer by providing a larger volume fraction of electrolyte. The water saturation in the Zirfon separator is ~1 (i.e., fully imbibed with electrolyte) and independent of current density due to its hydrophilicity (Fig. S3). The other factor impacting the ohmic resistance is the contact resistance, which is the most dominant factor impacting ohmic resistances in the electrodes. The contact resistance of the foam was fitted to a value of 12 $m\Omega\ cm^2$ whereas the contact resistance for the nickel-felt was fitted to a value of 3 $m\Omega\ cm^2$ due to the more compact fibers and higher surface area for contact with the flow plate. Collectively, these results highlight how electrodes with higher surface area and lower contact resistances enable more efficient water electrolysis.

Crossover of H_2 gas at low current densities is a safety issue for any electrolyzer, and especially LAWEs due to their porous separator. To analyze this effect, we compare the mole fraction of H_2 in O_2 in the anode compartment to data collected by Haug et al.[38] for experiments performed with separated electrolyte cycles (*i.e.,* no mixing of anodic and cathodic electrolytes) at the same operating conditions as our cell experiments (1 bar; 80 °C). While the nickel electrodes in the study by Haug et al. are slightly different than the ones used in this work, we do not observe a significant dependence of H_2 crossover on electrode properties (the fraction of H_2 in O_2 perfectly overlap for our simulations of nickel-foam and nickel-felt electrodes). This result is expected, since at a constant current density the same amount of gas is produced at both electrodes regardless of the electrode structure and properties. Thus, the gas crossover rate is predominantly governed by the separator properties and the solubility of gas (which depends on the concentration of KOH and temperature of the electrolyzer). Overall, the results show good agreement between the modeled and experimental values (Fig. 2d). Moreover, the H_2 in O_2 mole fraction was found to be below the lower flammability limit for H_2 (4%). However, the H_2 in O_2 mole fraction does approach 1% at current densities less than 0.01 A cm^{-2}, indicating that a minimum current density must be respected during load cycling to prevent safety issues.

Simulated concentration and flux profiles.—The model affords the opportunity to examine the different concentration profiles within the LAWE. The results show that the consumption and generation of OH^- by the OER and HER, respectively, induce a concentration gradient across the cell (Figs. 3a, 3b). The consumption of OH^- reduces the rate of OER because of the first-order dependence of this reaction on OH^-.[39] Moreover, the bulk ionic

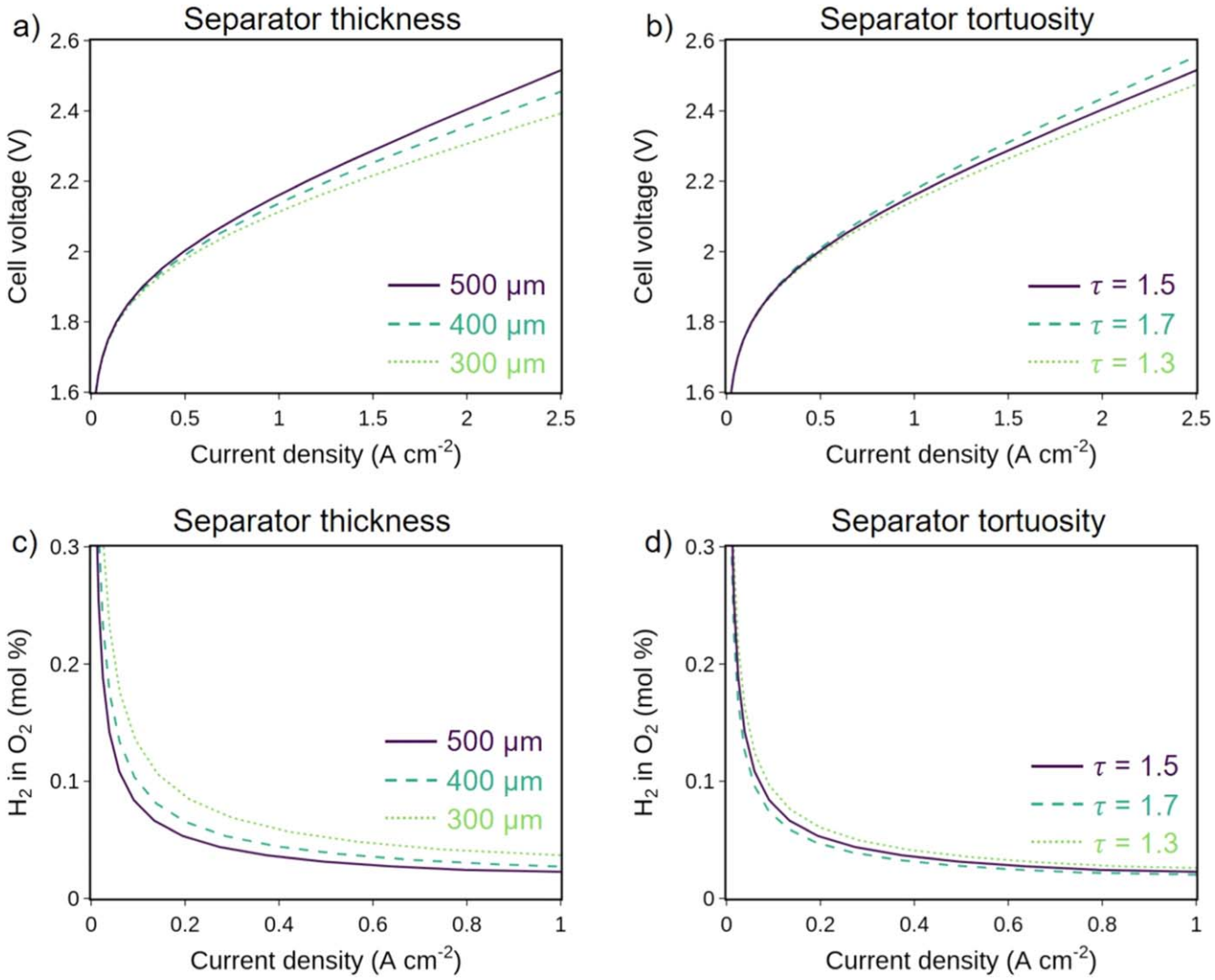

Figure 4. Sensitivity analyses showing the effect of separator (a) thickness and (b) tortuosity on polarization behavior of LAWEs. Effect of separator (a) thickness and (d) tortuosity on the H_2 in O_2 within the anode compartment.

conductivity is reduced in both the anode and cathode due to the deviation in KOH concentration from the bulk value of 7 M (Fig. 3 c).[12] The water activity also deviates from the bulk value of 0.61, which shifts the equilibrium potential of the reactions (Fig. 3d). Together, these gradients in pH and water activity make the equilibrium potential of the HER more negative by ~60 mV and the equilibrium potential of OER more positive by ~40 mV at 2 A cm^{-2}, as per the Nernst equation. Compared to 0-D models,[7] the model herein can resolve these spatial gradients and thus account for changes in the equilibrium potential of the anode and cathode reactions, something that 0-D models cannot. Furthermore, this 1-D model is exploring how the local conditions impact the equilibrium half-cell reactions to elucidate which electrode is responsible for the majority of losses in the cell.

To understand the dominant modes of transport in the electrolyzer, one can look at the liquid-phase Péclet number (Pe) and fluxes of OH^- (Fig. S4). Throughout the separator, the Pe is zero (Fig. S4a) due to the low convective flux of OH^- (Fig. S4b), which arises from the low permeability of Zirfon ($7.5x10^{-16}$ m^2).[6] The convective flux of OH^- in the electrodes increase with increasing current density due to the production of dissolved H_2 and O_2 and subsequent mass-transfer from the liquid to the gas phase. A larger convective flux is observed in the anode than the cathode because of the larger mass loss from the liquid-phase associated with O_2 evolution compared to H_2 evolution. The asymptotes observed in the Pe are caused by the peak in OH^- concentration within the electrodes (Fig. 3a), where the diffusive flux of OH^- is zero (Fig. S4c). Within the separator, the diffusive flux of OH^- is negative (*i.e.,* diffusional transport is from cathode to anode), indicating that diffusion of OH^- contributes positively to the current density in the liquid-phase. However, the dominant mechanism for OH^- transport in the separator is migration (Fig. S4d), which accounts for ~91% of the total OH^- flux.

The liquid-phase pressure is practically constant across the electrolyzer because of the high permeability and water saturation of the electrodes (Fig. S5a). The liquid-phase mass-averaged velocities are positive in the anode and negative in the cathode, indicating that liquid is flowing into the cell (Fig. S5b). The gas pressure in the electrodes increases as the current density is increased due to the production of O_2 and H_2 gas (Fig. S5c). The mass-averaged velocity of the gas-phase (Fig. S5d) is significantly higher than that of the liquid-phase because of the lower density of H_2 and O_2 compared to the KOH electrolyte. This gas-velocity is negative in the anode and positive in the cathode, indicating that bubbles formed from OER and HER transport out of the electrolyzer by convection.

Applied-voltage-breakdown and sensitivity analyses.—The total cell potential was decomposed into its constituent components using the power-loss-analysis technique introduced by Secanell et al.[40,41] (Figure S6). Higher kinetic overpotentials are observed for OER

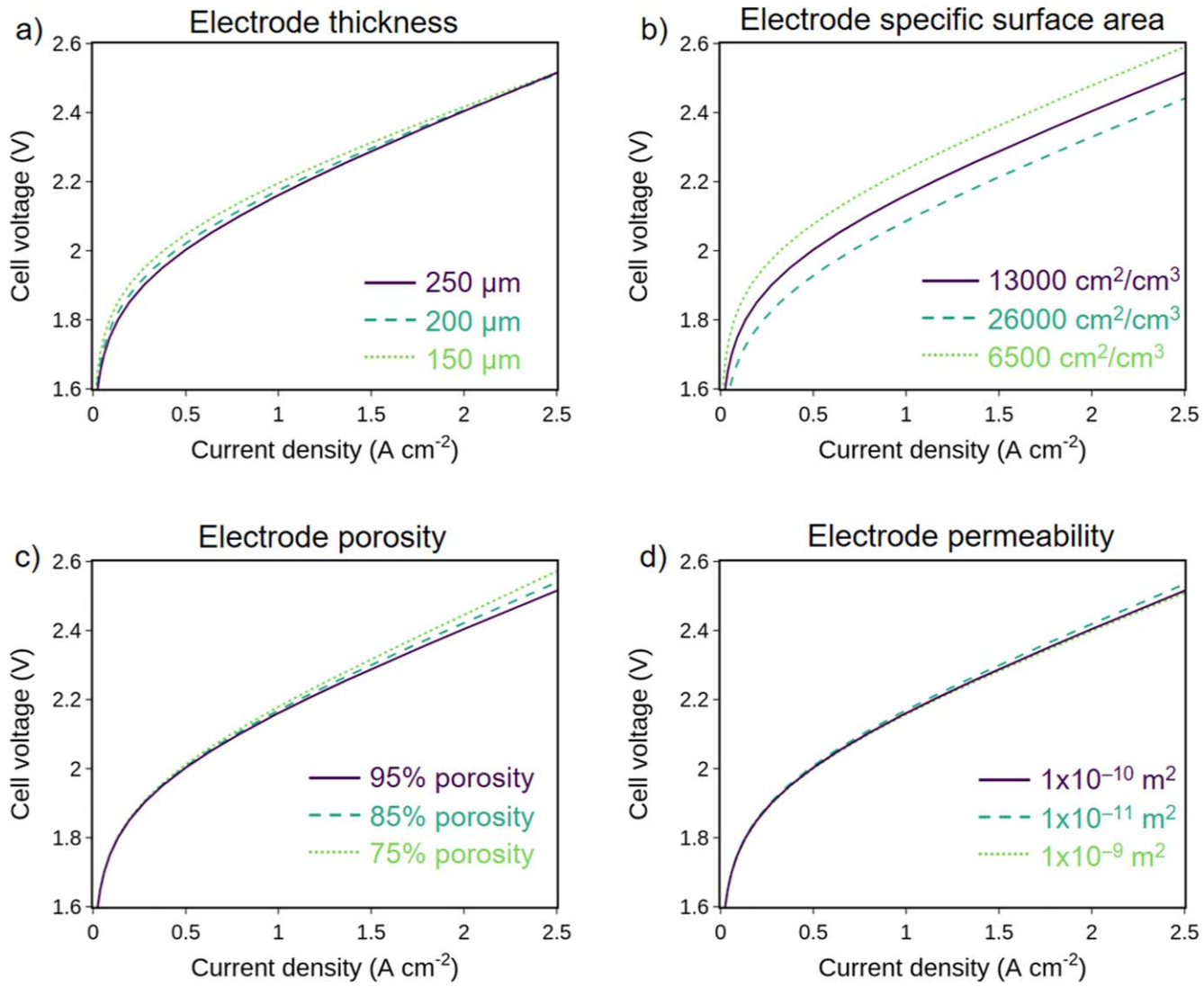

Figure 5. Sensitivity analyses showing the effect of electrode (a) thickness, (b) specific surface area, (c) porosity, and (d) permeability on LAWE polarization behavior.

than HER, but the HER overpotentials are still significant because of the highly-alkaline conditions. This result is consistent with the work of Haverkort et al.[29] and highlights the importance of a spatially-resolved model. Bubble resistances were found to contribute ∼20 mV to the total applied potential at 2 A cm^{-2}. The modeled ohmic resistance in the separator is a primary contributor to the total applied voltage, and this model result matches well with the EIS measured ohmic drop (Fig. 2). These results point to the need to develop improved electrode and separator architectures to improve LAWE performance.

To determine methods for reducing ohmic resistances, we simulated the effect of reducing the separator thickness and tortuosity on the polarization behavior (Fig. 4). The results show a dramatic improvement in current density when the separator thickness is reduced from 500 to 300 µm (Fig. 4a). A reduction in separator tortuosity from 1.5 to 1.3 also decreases the cell potential, but to a lesser extent than reducing the separator thickness (Fig. 4b). While reducing the separator thickness and tortuosity is shown to improve electrolysis performance, these improvements come at the expense of increase H_2 crossover (Figs. 4c, 4d).

The optimization of electrodes properties is complicated by trade-offs between ohmic and kinetic overpotentials in different current-density regimes. For example, the simulation shows that thinner electrodes reduce the current density of the electrolyzer at voltages < 2 V (Fig. 5a). Kinetic overpotentials are dominant in this regime, and therefore, the thinner electrodes perform worse than the thicker electrodes due to a lower surface area for HER and OER. This is consistent with the sensitivity analysis on specific surface area, which shows that a 2x increase in specific surface area leads to a significant increase in current density (Fig. 5b). At cell potentials > 2 V, the thinner electrodes achieve similar current densities as the thicker electrodes because the resistance in the liquid-phase results in the reaction distribution being shifted to next to the electrolyte/separator interface and thus essentially the same amount of electrode is being utilized. In this potential regime, the reduction in ohmic resistances enabled by thinner electrodes is offset by the larger kinetic overpotential associated with a lower surface area.

The model shows that decreasing the electrode porosity from 95% to 75% increases the applied voltage required to achieve current densities >1 A cm^{-2} due to increased ohmic resistances associated with ion transport in the electrodes (Fig. 5c). Decreasing the permeability of the electrodes also results in a higher applied voltage at high current densities (Fig. 5d). Since convection is not a dominant mechanism of ion transport in the electrodes (Fig. S4a), the permeability of the electrodes mostly impacts the rate of gas-transport out of the electrolyzer. Therefore, the modest improvement

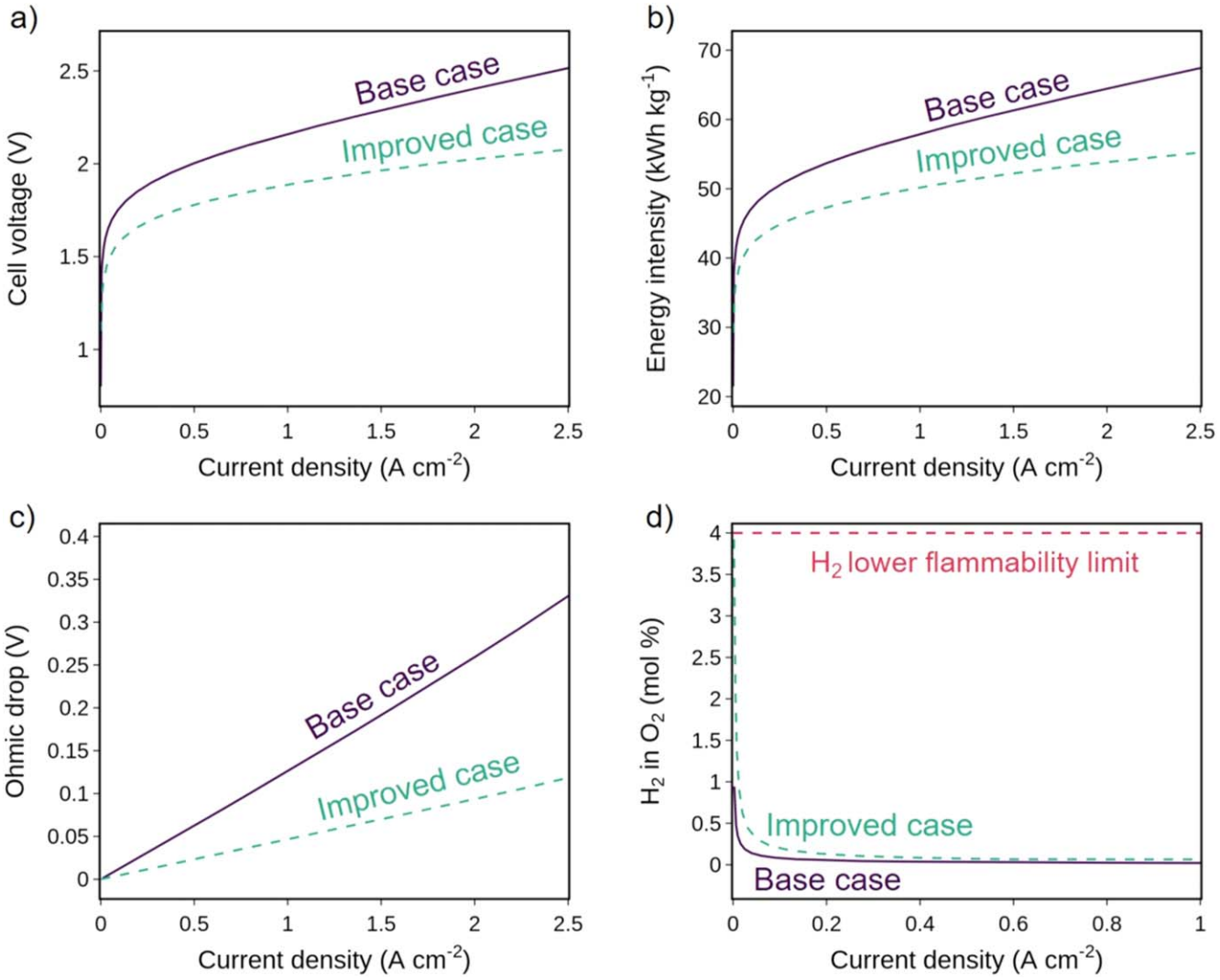

Figure 6. Simulated (a) current densities, (b) energy-intensities, (c) ohmic drops, and (d) H_2 in O_2 anodic mole fractions for the LAWE tested in this study using nickel-felt electrodes (denoted: "Base case") and a theoretically-optimized electrolyzer (denoted: "Improved case") with electrodes exhibiting 5x the specific surface area of the Base case and a 5x thinner separator.

in performance with more permeable electrodes is a result of increased water saturation in the electrodes, which reduces ohmic resistances.

The energy intensity of H_2 production (expressed in terms of kWh kg^{-1}) is a key metric, which defines the technoeconomic feasibility of water electrolyzers. The applied-voltage-breakdown and sensitivity analyses point to separator thickness and electrode surface area as the key factors that determines the performance of LAWE. We therefore investigated whether modulating these two key parameters could enable LAWEs to achieve a benchmark energy intensity for H_2 production of 50 kWh kg^{-1}, which is a key target for low temperature water electrolysis.[5]

The "Base case" simulation obtained with nickel-felt electrodes shows that a current density of 1 A cm^{-2} is achieved at ~2.17 V (corresponding to an energy intensity >57 kWh kg^{-1}) (Figs. 6a, 6b). The "Improved case," which was simulated with a 5x higher specific surface area (*i.e.,* 65000 cm^2/cm^3) and 5x thinner separator (*i.e.,* 100 μm) than the "Base case," was found to enable a current density of 1 A cm^{-2} at 1.87 V, corresponding to an energy intensity of 50 kWh kg^{-1} at 1 A cm^{-2}. A primary factor in achieving this improved performance is the reduction in ohmic drop, which is made possible by the thinner separator (Fig. 6c). However, this use of a thinner separator is predicted to increase the H_2 in O_2 to dangerous levels at low current densities (Fig. 6c). This tradeoff could be overcome by engineering the mixture of polysulfone and metal-oxide precursors used to synthesize LAWE separators that maximize ionic conductivity while mitigating H_2 crossover.[42] Moreover, the enhanced electrode surface area simulated here may be achievable with coatings or nanoparticles deposited on the nickel-felt surface. Collectively, these results demonstrate that LAWEs are capable of achieving energy-intensities rivaling PEMWEs by modulating the specific surface area of the electrodes and thickness of the separator, but new approaches to separator design including the use of gas-recombination catalysts are necessary to realize this performance.[43]

Model limitations.—The 1-D model reported here encompasses physics that accurately capture the Ohmic resistances and thermodynamics of the half-cell reactions. However, the model neglects the kinetics and dynamics of bubble nucleation and flow within the electrode by assuming the gas- and liquid-flows obey Darcy's Law (i.e., continuous phases), likely leading to an underestimation of the effect of bubble formation and coverage on overpotentials. This limitation of the model may lead to inaccurate fitting of the exchange current densities in this work, as the effective specific surface area directly correlates with the half-cell reaction rates. Notwithstanding, more sophisticated models and experimental analysis of bubble formation in LAWEs show that the effect of bubbles constitutes only 4% to the total overpotential at 0.5 A cm^{-2} (similar to the results

shown in Fig. S6).[44] Thus, we do not expect this model limitation to impact the results of this study significantly. Furthermore, the model treats the wettability of the porous media with a constant property (i.e., contact angle) that could change due to pore shape and chemistry,[45] and thus the model can be improved with measured capillary-pressure/saturation curves that is a current area of research.

Summary

In this study, a continuum model is developed and used to deconvolute energy losses and investigate the effect of material properties on liquid-alkaline water electrolyzer (LAWE) performance. The model shows that gradients within the electrodes lead to a Nernstian-shift that increase the equilibrium potential of the oxygen-evolution reaction (OER) while reducing the equilibrium potential for the hydrogen-evolution reaction HER. H_2 and O_2 gases that are formed by the electrode reactions are shown to be concentrated near the electrode/separator interfaces, thereby increasing the kinetic overpotentials by reducing the surface area in contact with the electrolyte and increasing ohmic overpotentials by increasing ionic-transport tortuosities. Sensitivity analyses show that reducing the separator thickness and increasing the surface area of nickel electrodes are promising means of increasing LAWE performance, but new approaches for separator design must be devised to manage crossover in thinner separators. This study underscores the importance and value of using spatially-resolved models to identify, quantify, and mitigate energy losses in LAWEs.

Acknowledgments

This material is based on work performed within the H2New consortium, which is supported by the U.S. Department of Energy, Office of Energy Efficiency and Renewable Energy, Hydrogen and Fuel Cell Technologies Office under contract DE-AC02–05CH11231. EWL would like to acknowledge support from the National Science and Engineering Research Council (NSERC) Post-doctoral fellowship. J.C.B. was supported in part by a fellowship award under contract FA9550–21-F-0003 through the National Defense Science and Engineering Graduate (NDSEG) Fellowship Program, sponsored by the Army Research Office (ARO). H.R.B. acknowledges funding from a National Science Fellowship Graduate Research Fellowship.

ORCID

Eric W. Lees https://orcid.org/0000-0002-0524-3816
Justin C. Bui https://orcid.org/0000-0003-4525-957X
Guanhzi Wang https://orcid.org/0000-0002-5094-5630
Xiong Peng https://orcid.org/0000-0001-8737-5830
Alexis T. Bell https://orcid.org/0000-0002-5738-4645
Adam Z. Weber https://orcid.org/0000-0002-7749-1624

References

1. T. R. Cook et al., "Solar energy supply and storage for the legacy and non legacy worlds." *Chem. Rev.*, **110**, 6474 (2010).
2. T. Lehtola and A. Zahedi, "Solar energy and wind power supply supported by storage technology: a review." *Sustainable Energy Technologies and Assessments*, **35**, 25 (2019).
3. A. Buttler and H. Spliethoff, "Current status of water electrolysis for energy storage, grid balancing and sector coupling via power-to-gas and power-to-liquids: a review." *Renewable Sustainable Energy Rev.*, **82**, 2440 (2018).
4. E. Lewis et al., *Comparison of Commercial, State-of-the-Art, Fossil-Based Hydrogen Production Technologies*, United States (2022), https://www.osti.gov/biblio/1862910.
5. B. Pivovar, M. Ruth, and R. Ahluwalia, *Report Number: NREL/PR-6A20-82706*, United States (2022), https://www.osti.gov/biblio/1900160.
6. M. Schalenbach et al., "Acidic or Alkaline? towards a new perspective on the efficiency of water electrolysis." *J. Electrochem. Soc.*, **163**, F3197 (2016).
7. P. Trinke et al., "Hydrogen crossover in PEM and Alkaline water electrolysis: mechanisms, direct comparison and mitigation strategies." *J. Electrochem. Soc.*, **165**, F502 (2018).
8. H. Kojima et al., "Influence of renewable energy power fluctuations on water electrolysis for green hydrogen production." *Int. J. Hydrogen Energy*, **48**, 4572 (2023).
9. M. T. de Groot and A. W. Vreman, "Ohmic resistance in zero gap alkaline electrolysis with a Zirfon diaphragm." *Electrochim. Acta*, **369**, 137684 (2021).
10. C. Henao et al., "Simulation tool based on a physics model and an electrical analogy for an alkaline electrolyser." *J. Power Sources*, **250**, 58 (2014).
11. A. Iribarren et al., *2021 IEEE International Conference on Environment and Electrical Engineering and 2021 IEEE Industrial and Commercial Power Systems Europe (EEEIC / I&CPS Europe), 2021, pp. 1–6*.
12. J. N. Hausmann et al., "The pH of aqueous NaOH/KOH solutions: a critical and non-trivial parameter for electrocatalysis." *ACS Energy Lett.*, **6**, 3567 (2021).
13. C. Karacan et al., "Challenges and important considerations when benchmarking single-cell alkaline electrolyzers." *Int. J. Hydrogen Energy*, **47**, 4294 (2022).
14. G. C. Akerlof and P. Bender, "Thermodynamics of aqueous solutions of potassium hydroxide." *JACS*, **70**, 2366 (1948).
15. G. Akerlof and G. Kegeles, "Thermodynamics of concentrated aqueous solutions of sodium hydroxide." *JACS*, **62**, 620 (1940).
16. G. Akerlof and P. Bender, "The density of aqueous solutions of potassium hydroxide." *JACS*, **63**, 1085 (1941).
17. A. Hodges et al., "Critical analysis of published physical property data for aqueous potassium hydroxide. collation into detailed models for alkaline electrolysis." *J. Chem. Eng. Data*, **68**, 1485 (2023).
18. L. C. Weng, A. T. Bell, and A. Z. Weber, "Modeling gas-diffusion electrodes for CO2 reduction." *Phys. Chem. Chem. Phys.*, **20**, 16973 (2018).
19. J. T. Kraakman, *Gas Crossover in Liquid Alkaline Electrolysis*, Eidenhoven University of Technology (2023), https://pure.tue.nl/ws/portalfiles/portal/295806633/MCE_afstudeerverslag_Joost_Kraakman_1012891_.pdf.
20. L. J. J. Janssen and J. G. Hoogland, "The effect of electrolytically evolved gas bubbles on the thickness of the diffusion layer—II." *Electrochim. Acta*, **18**, 543 (1973).
21. L. J. J. Janssen and J. G. Hoogland, "The effect of electrolytically evolved gas bubbles on the thickness of the diffusion layer." *Electrochim. Acta*, **15**, 1013 (1970).
22. E. N. Fuller, P. D. Schettle, and J. C. Giddings, "A new method for prediction of binary gas-phase diffusion coeffecients." *Ind. Eng. Chem.*, **58**, 19 (1966), -+.
23. P. S. Liu and K. M. Liang, "Evaluating electrical resistivity for high porosity metals." *Mater. Sci. Technol.*, **16**, 341 (2000).
24. J. C. Ehlers, A. A. Feidenhans'l, K. T. Therkildsen, and G. O. Larrazábal, "Affordable green hydrogen from alkaline water electrolysis: key research needs from an industrial perspective." *ACS Energy Lett.*, **8**, 1502 (2023).
25. J. W. Haverkort and H. Rajaei, "Electro-osmotic flow and the limiting current in alkaline water electrolysis." *Journal of Power Sources Advances*, **6** (2020).
26. R. J. Gilliam, J. W. Graydon, D. W. Kirk, and S. J. Thorpe, "A review of specific conductivities of potassium hydroxide solutions for various concentrations and temperatures." *Int. J. Hydrogen Energy*, **32**, 359 (2007).
27. J. Rodriguez et al., "Simple and precise approach for determination of ohmic contribution of diaphragms in alkaline water electrolysis." *Membranes*, **9** (2019).
28. J. Chen et al., "Calculation method of specific surface area of foam metal based on an ideal tetradecahedron model for lithium ion battery." *Int. J. Photoenergy*, **2020** (2020).
29. J. W. Haverkort and H. Rajaei, "Voltage losses in zero-gap alkaline water electrolysis." *J. Power Sources*, **497** (2021).
30. J. Brauns and T. Turek, "Alkaline water electrolysis powered by renewable energy: a review." *Processes*, **8** (2020).
31. M. Hammoudi et al., "New multi-physics approach for modelling and design of alkaline electrolyzers." *Int. J. Hydrogen Energy*, **37**, 13895 (2012).
32. A. Z. Weber and J. Newman, "Modeling transport in polymer-electrolyte fuel cells." *Chem. Rev.*, **104**, 4679 (2004).
33. S. Huo et al., "Elucidating the operating behavior of PEM fuel cell with nickel foam as cathode flow field." *Sci. China Technol. Sci.*, **64**, 1041 (2021).
34. M. Zlobinski et al., "Transient and steady state two-phase flow in anodic porous transport layer of proton exchange membrane water electrolyzer." *J. Electrochem. Soc.*, **167** (2020).
35. M. R. Gerhardt et al., "Method-practices and pitfalls in voltage breakdown analysis of electrochemical energy-conversion systems." *J. Electrochem. Soc.*, **168** (2021).
36. M. Schalenbach et al., "How microstructures, oxide layers, and charge transfer reactions influence double layer capacitances. Part 1. Impedance spectroscopy and cyclic voltammetry to estimate electrochemically active surface areas (ECSAs)." *Phys. Chem. Chem. Phys.*, **26**, 14288 (2024).
37. S. L. Medway et al., "In situ studies of the oxidation of nickel electrodes in alkaline solution." *J. Electroanal. Chem.*, **587**, 172 (2006).
38. P. Haug, B. Kreitz, M. Koj, and T. Turek, "Process modelling of an alkaline water electrolyzer." *Int. J. Hydrogen Energy*, **42**, 15689 (2017).
39. J. J. Liu et al., "Elucidating the role of hydroxide electrolyte on anion-exchange-membrane water electrolyzer performance." *J. Electrochem. Soc.*, **168** (2021).
40. M. Secanell et al., "Mathematical modelling and experimental analysis of thin, low-loading fuel cell electrodes." *ECS Trans.*, **69**, 157 (2015).
41. A. Kosakian, L. P. Urbina, A. Heaman, and M. Secanell, "Understanding single-phase water-management signatures in fuel-cell impedance spectra: a numerical study." *Electrochim. Acta*, **350**, 136204 (2020).
42. H. I. Lee et al., "Advanced Zirfon-type porous separator for a high-rate alkaline electrolyser operating in a dynamic mode." *J. Membr. Sci.*, **616** (2020).
43. A. Stähler et al., "Scalable implementation of recombination catalyst layers to mitigate gas crossover in PEM water electrolyzers." *J. Electrochem. Soc.*, **169**, 034522 (2022).
44. X. T. Deng et al., "Quantitative study on gas evolution effects under large current density in zero-gap alkaline water electrolyzers." *J. Power Sources*, **555**, 232378 (2023).
45. A. Z. Weber, "Improved modeling and understanding of diffusion-media wettability on polymer-electrolyte-fuel-cell performance." *J. Power Sources*, **195**, 5292 (2010).